GENETICS

A single locus regulates a female-limited color pattern polymorphism in a reptile

Nathalie Feiner[1]*, Miguel Brun-Usan[1], Pedro Andrade[2,3], Robin Pranter[1], Sungdae Park[4], Douglas B. Menke[4], Anthony J. Geneva[5], Tobias Uller[1]

Animal coloration is often expressed in periodic patterns that can arise from differential cell migration, yet how these processes are regulated remains elusive. We show that a female-limited polymorphism in dorsal patterning (diamond/chevron) in the brown anole is controlled by a single Mendelian locus. This locus contains the gene *CCDC170* that is adjacent to, and coexpressed with, the *Estrogen receptor-1* gene, explaining why the polymorphism is female limited. *CCDC170* is an organizer of the Golgi-microtubule network underlying a cell's ability to migrate, and the two segregating alleles encode structurally different proteins. Our agent-based modeling of skin development demonstrates that, in principle, a change in cell migratory behaviors is sufficient to switch between the two morphs. These results suggest that *CCDC170* might have been co-opted as a switch between color patterning morphs, likely by modulating cell migratory behaviors.

INTRODUCTION

Periodic color patterns provide an outstanding opportunity to study how genetic regulation of the dynamical properties of individual cells can give rise to collective behaviors and distinctive phenotypes. Different developmental mechanisms have been proposed to be capable of creating such periodicity. One of the simplest is the Turing mechanism (*1*), a type of reaction-diffusion process that consists of two gene products that interact as activator and inhibitor and that exhibit differential diffusion and binding affinities (*2*). When implemented in a two-dimensional (2D) surface, the outcomes of such models capture actual animal skin patterns surprisingly well (*3*–*5*). In addition, these models produce periodic patterns from stochastic initial conditions and are often robust against perturbations, which are common features of biological systems (*2*). These observations, along with the simplicity of Turing systems, have led to the hypothesis that most periodic color patterns in vivo also result from Turing-type mechanisms involving the interaction and self-organization of different cell types during development. Although the identities of the activator and inhibitor molecules typically remain unknown [but see, e.g., (*5*, *6*)], the presence of Turing-type mechanisms is supported by studies on morphological structures [e.g., digits (*7*), cusps of mammalian teeth (*8*), and scutes of turtle carapaces (*9*)] and color patterning [e.g., stripes of zebrafish (*10*, *11*) and dots and stripes in mammalian coats (*12*, *13*)]. Yet, how the patterning process is regulated at the genetic level, how this translates into complex cell behaviors, and how transitions from one pattern to another occur throughout evolution remain open questions.

In vertebrates, pigment cells are derived from neural crest cells that originate along the dorsal midline of the early embryo (*14*–*16*). Once detached from the crest of the neural tube, pigment cell precursors migrate toward their final destination in the epidermis using a variety of structural and biochemical cues (*17*). Cell migration is enabled by a polarization of the Golgi-microtubule network that leads to an asymmetric cell shape with more active pseudopodia at the leading edge, promoting directed cell movement (*18*). Thus, the position and differentiation state of a pigment cell in the developing embryo can depend on both the morphogen distribution (potentially determined by a Turing-type mechanism) and its morphogenetic cell migration (determined by cell polarity and motility).

The occurrence of multiple, discrete color patterns in a single species—pattern polymorphism—enables us to establish the genetic basis of such pattern variation and the transition from one pattern to another. Several species of *Anolis* lizards have independently evolved a conspicuous female-limited polymorphism in dorsal skin patterning (*19*). In the brown anole lizard (*Anolis sagrei*), females exhibit either diamond- or chevron-like dorsal patterns, while males invariably show the chevron-like pattern (Fig. 1). Taking advantage of this naturally occurring variation, we established the genetic basis of this female-limited pattern polymorphism to derive from allelic variation at a single locus affecting a cytoskeleton-associated protein, CCDC170, known to promote (ON) or disrupt (OFF) cell migration. Agent-based mathematical modeling supports that modification of the migratory capacity of individual cells can result in alternative collective cell behaviors that can qualitatively reproduce diamond and chevron patterning. Such a simple genetic architecture of cell behavior may explain the frequent evolutionary transitions between these patterns in reptiles.

RESULTS

Genetic mapping of the diamond-chevron pattern polymorphism identifies a single autosomal locus

To unravel which changes in cell behavior lead to transitions between diamond and chevron patterning, we first addressed the genetic basis of the female-limited polymorphism. To this end, we conducted whole-genome pool sequencing of females of both morphs from three consecutive generations (field-caught F0 and laboratory-reared F1 and F2; average pool sizes: 25.17 individuals). Given the discreteness of the diamond and chevron morphs, we predicted a simple genetic architecture with one or few loci of major effect, and we reasoned

[1]Department of Biology, Lund University, Lund, Sweden. [2]CIBIO/InBIO Research Centre in Biodiversity and Genetic Resources, University of Porto, Campus Agrário de Vairão, Vairão, Portugal. [3]BIOPOLIS Program in Genomics, Biodiversity and Land Planning, CIBIO, Campus de Vairão, Vairão, Portugal. [4]Department of Genetics, University of Georgia, Athens, GA, USA. [5]Department of Biology and Center for Computational and Integrative Biology, Rutgers University–Camden, Camden, NJ, USA.
*Corresponding author. Email: nathalie.feiner@biol.lu.se

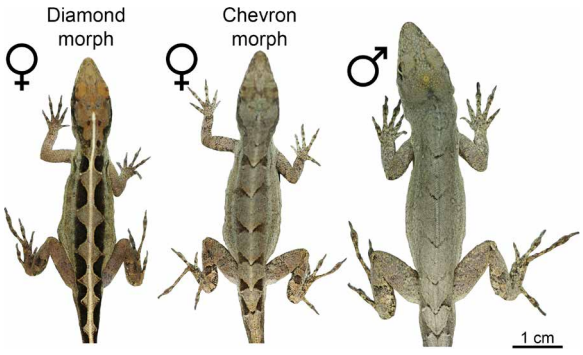

Fig. 1. Female-limited pattern polymorphism in *A. sagrei*. Females of the diamond morph show diamond-like markings characterized by light inner and dark outer areas with a contrast-enhancing boundary in between. Within the diamond morph, a broad and continuous variation in the shape of the diamonds exists, with the most extreme variants approaching a stripe (fig. S1) (*60*). Females of the chevron morph and all males of this species exhibit chevron-like markings. Note that *Anolis* lizards can exhibit physiological color change, but morph identity remains distinct and unchanged from the time pigmentation first arises, around embryonic stage 17 (*52*).

that contrasting across generations should increase the power to detect these loci (*20*). The combination of several statistical measures revealed a 44-kb locus on chromosome 1 that is completely associated with the diamond and chevron phenotypes (Fig. 2, A to C, and fig. S2). Despite the distinct boundaries of the candidate region, we find no evidence that this genetic polymorphism is maintained by an inversion (table S1). Within the 44-kb candidate region, the major allele frequencies of all chevron morph pools approached 1, while diamond pools showed lower major allele frequencies and increased nucleotide diversity (Fig. 2, D and E), consistent with the presence of two alleles.

These results led us to hypothesize a Mendelian dominant-recessive mode of inheritance, with the diamond (D) allele being dominant over the chevron (c) allele and therefore all chevron lizards being homozygous. We confirmed this genetic architecture by genotyping all 151 females that were included in the association study at a single SNP (single-nucleotide polymorphism) in the candidate region and found that 98.01% of phenotypic morphs were correctly predicted by the allelic variant of this single SNP (Fig. 3A). Mendelian inheritance of the pattern was confirmed using a pedigree of eight breeding groups of wild-caught *A. sagrei* (for one example, see Fig. 3B; for full information, see fig. S3).

The segregating alleles are evolutionarily young but code for structurally different proteins

The 44-kb candidate region spans six exons of the gene *CCDC170*, which encodes a protein containing coiled-coil domains. *CCDC170* is located next to the gene *ESR1* encoding the estrogen receptor 1 that is a key regulator of sexual development (Fig. 2C). A molecular phylogeny of reptile and bird *CCDC170* genes suggests that the diamond and chevron alleles are likely specific to *A. sagrei* (Fig. 3C and fig. S4), but sequence data of more closely related *Anolis* species could potentially identify more variants. Despite this relatively recent evolutionary origin, the coding region of *CCDC170* differs between the diamond and the chevron allele in 7 synonymous and 13 nonsynonymous sites (3 of the latter are caused by two mutations per codon; table S2). Both alleles have 11 exons, and we find no indication

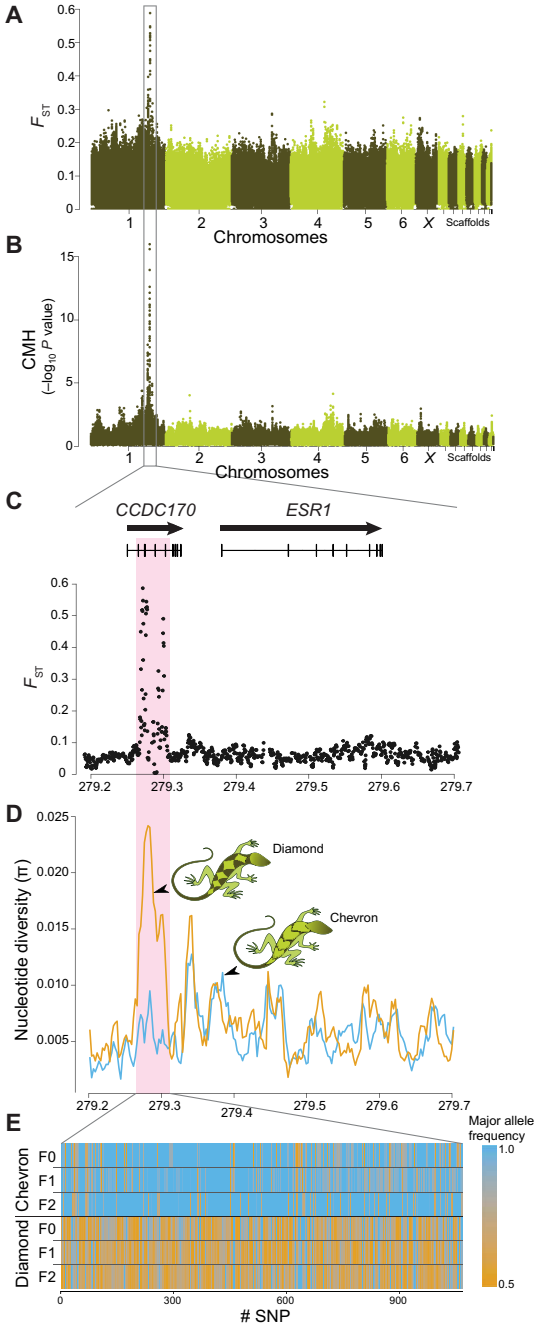

Fig. 2. Genetic mapping of the diamond-chevron pattern polymorphism. (**A**) Genetic differentiation (using the fixation index F_{ST}) between diamond and chevron morphs across the genome. F_{ST} values shown are the median of three intra-generational contrasts. (**B**) *P* values (–$\log_{10}$-transformed) of Cochran-Mantel-Haenszel (CMH) tests for consistent differences in allele frequencies between the morphs across the three generations. (**C**) Close-up view of the region marked in (A) and (B) and showing F_{ST} values similar to (A). The position of exons belonging to the genes *CCDC170* and *ESR1* are indicated on top, and the 44-kb candidate region is shaded in magenta. (A to C) Summary of individual variants in 100-SNP windows with 25-SNP steps (for individual SNPs in the candidate region, see fig. S2). (**D**) Nucleotide diversity π within the pools of chevron and diamond morphs of the F1 generation ($N = 97$) for the same region as in (C). (**E**) SNP panel showing the major allele frequencies of all variable SNPs ($N = 1067$) in the candidate region for each pool (SNPs close to fixation were excluded; see Materials and Methods).

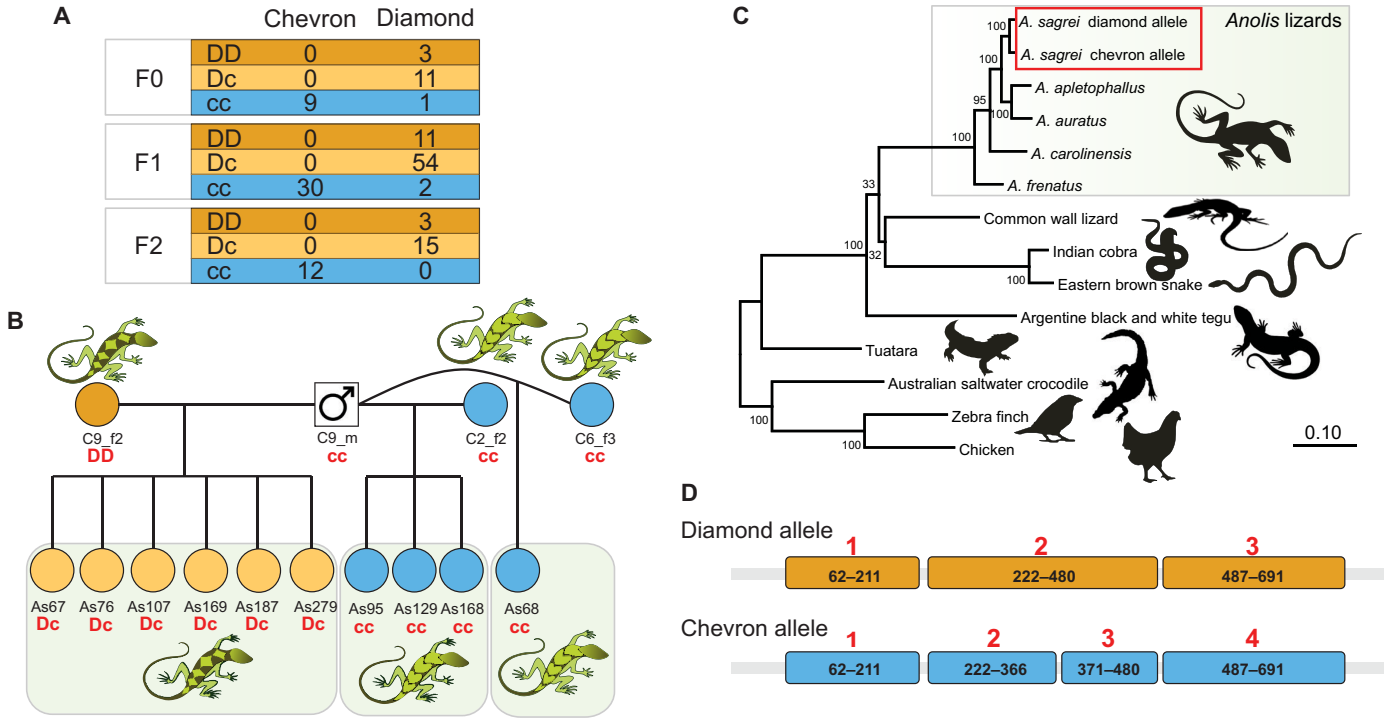

Fig. 3. Two alleles at the *CCDC170* locus genetically determine the diamond-chevron pattern polymorphism. (**A**) Genotype distribution of individuals of all six pools used in the whole-genome pool sequencing. Genotypes were inferred on the basis of a single SNP in exon 2 of the *CCDC170* gene. (**B**) A representative pedigree, with one male and three females, for which phenotypes and genotypes of each individual of the parental generation and of all female offspring were determined. Individual genotypes are indicated in red font, and phenotypes are indicated by schematic drawings (light green boxes mark full siblings). Pedigrees for seven other breeding groups can be found in fig. S3. The observed distribution of morphs and genotypes follows a dominant-recessive mode of inheritance, with the diamond allele being dominant over the chevron allele. (**C**) Maximum likelihood tree showing the phylogenetic relationships between the two *CCDC170* alleles of *A. sagrei* and orthologs in other *Anolis* species (green box) and more distantly related reptiles and birds (based on 765 amino acid residues and using a JTT + Γ_4 model). For accession numbers of sequences, see table S3. (**D**) Coiled-coil domain predictions of the two CCDC170 proteins derived from the two alleles. Colored boxes show the position of predicted coils, black numbers provide the amino acid positions included in each coil, and red numbers show the sequence number of each predicted coil (see fig. S5 for more details on domain predictions).

of alternative splicing (GenBank accession IDs: MZ268124 and MZ268125). Domain prediction of the resulting protein sequences suggests that the nonsynonymous changes translate into a difference in the folding of the coiled-coil domains (three domains are predicted for the diamond allele, and four are predicted for the chevron allele; Fig. 3D and fig. S5) that are known to affect dimerization and thus function of CCDC (coiled-coil domain-containing) proteins (*21*).

CCDC170 expression levels do not differ between female morphs but are consistently lower in males

After having established coding changes between the two *CCDC170* alleles, we tested whether both alleles are expressed during pattern formation in dorsal epithelial tissue. Using quantitative polymerase chain reaction (qPCR), we found that *CCDC170* is indeed expressed in dorsal epithelial tissue of female embryos, but expression levels between the three *CCDC170* genotypes (cc, Dc, and DD) did not differ ($N_{individuals}$ = 19, P = 0.89; Fig. 4B, fig. S6, and table S4). This indicates that regulatory changes in *CCDC170* are unlikely to explain the morph differences between female *A. sagrei*.

In humans, *CCDC170* is coexpressed with its neighboring gene *ESR1* (*22*). We hypothesized that the physical genetic linkage could cause higher expression in females than in males and therefore explain why the polymorphism is limited to females. We therefore tested whether the two genes are coexpressed also in *A. sagrei*. The main expression domain of *ESR1* was found in hemipenes, which are the external genitalia present in both male and female embryos at early stages but become sexually dimorphic at around developmental stage 9 (fig. S7). As expected, *ESR1* showed a strongly sex-biased expression with higher expression levels in females, and this effect was most pronounced in hemipenes (Fig. 4C, fig. S6, and table S4). A partial correlation, accounting for their reliance on normalization with the same housekeeping gene, revealed that *CCDC170* and *ESR1* expression levels are moderately, but significantly, correlated in the hemipenes (r = 0.42, P = 0.047, $N_{individuals}$ = 24) and strongly correlated in the dorsal epithelia (r = 0.73, P < 0.001, $N_{individuals}$ = 35; Fig. 4C). In agreement with this correlated expression between the two neighboring genes *CCDC170* and *ESR1*, we also find a sex-biased expression of *CCDC170* with lower expression levels in dorsal epithelia of male embryos ($N_{individuals}$ = 37, P = 0.048; Fig. 4C, fig. S6, and table S4). This indicates that the shared regulation of the *CCDC170-ESR1*-locus and the resulting low expression levels of *CCDC170* at the site of pattern formation in male embryos likely play causal roles in the pattern polymorphism being limited to females.

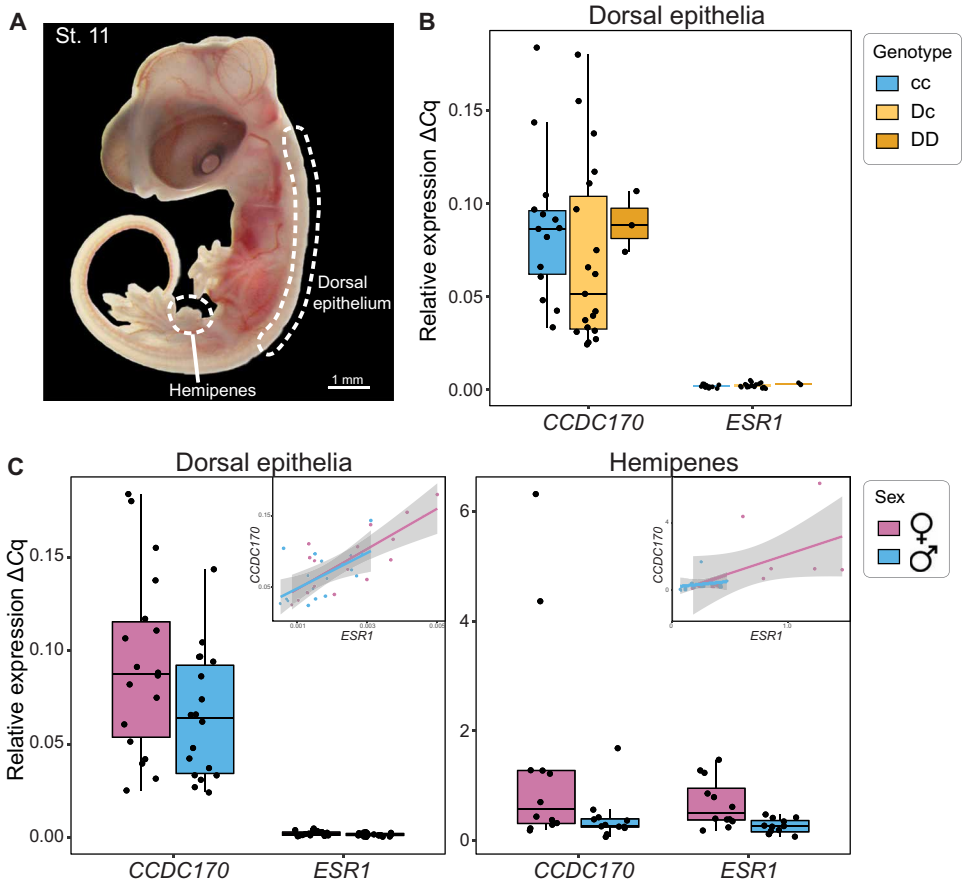

Fig. 4. Embryonic gene expression shows coexpression of *CCDC170* and *ESR1* in dorsal epithelia and hemipenes. (**A**) A representative *A. sagrei* embryo at developmental stage 11 illustrates the position of the microdissected tissue that was used in qPCR (see white dashed lines). (**B**) *CCDC170* expression levels in dorsal epithelia of female embryos are comparable between different *CCDC170* genotypes, while *ESR1* is consistently lowly expressed. (**C**) Expression of *CCDC170* and *ESR1* is positively correlated in both dorsal epithelia and hemipenes (see the main text and insets on the top right of each plot that show linear regressions for each sex with 95% confidence level intervals shaded in gray) and higher in females than in males. For expression patterns of both genes in hemipenes obtained by in situ hybridization, see fig. S7. qPCR experiments included a total of 37 embryonic samples, and expression levels were normalized relative to GAPDH (glyceraldehyde-3-phosphate dehydrogenase). Relative expression levels ΔCq were obtained by averaging quantification cycle (Cq) values of three technical replicates.

Previous studies suggest a role of CCDC170 in regulating cell migration

In vitro experiments have demonstrated that the CCDC170 protein plays an essential role in Golgi-associated microtubule organization, which has a critical impact on cytoskeletal dynamics and hence cell behaviors (e.g., cell polarity, emission of pseudopodia, and changes in cell shape) (*23*). Interfering with this cytoskeletal organization, in turn, can hinder the ability of cells to display directed cell migration including their ability to follow a chemical (i.e., morphogen) gradient (*23*). This role of the CCDC170 protein in cell polarity and motility, a hallmark of cancer cells, is hypothesized to explain why mutations resulting in truncated CCDC170 transcripts or ESR1-CCDC170 fusion proteins show a strong association with the risk for breast cancer in humans (*23*, *24*). Experimental validation that CCDC170 regulates cell migration in developing *Anolis* embryos would be an interesting, if methodologically challenging (*25*), avenue for future research. Nevertheless, on the basis of the genomic data, we hypothesized that allelic differences in *Anolis* CCDC170 proteins affecting cell migration are responsible for the difference between diamond and chevron morphs.

Agent-based modeling demonstrates that a single-locus genetic switch can be sufficient to transition between the two morphs

How could cell migration alone regulate the diamond and chevron pattern polymorphism? One possible mechanism is that the spatial distribution of the relevant cells (e.g., melanocytes) in the growing dorsal epithelium depends on the migratory behavior of epithelial cells themselves. Here, we establish a proof of principle that two alternative alleles of a single gene that regulate cell polarity or motility can be sufficient to reproduce the transition between both patterns.

To this end, we developed a cell-based computational model of the dynamic pattern formation processes in a growing 2D epithelium. To capture relevant dynamics of pattern formation, the model incorporates cellular behaviors but is not designed to recapitulate all aspects of pattern formation. Briefly, the model implements a large number ($1.5 \times 10^3 < N_C < 10^4$) of motile cells, each equipped with an identical gene regulatory network (GRN; Fig. 5A). Each GRN has a core patterning mechanism capable of breaking the initial homogeneity by establishing simple periodic patterns. While different mechanisms are conceivable [e.g., (*26*)], we implemented the simplest one,

which is a core Turing-type mechanism with one activator and one inhibitor gene (both with initial random expression). Because this core mechanism can only generate dots and stripes (*1*, *27*), we supplemented the GRN with up to three modulating genes initially expressed along simple gradients to assess whether diamond- or chevron-like patterns emerge.

We first identified six network topologies (NTs) able to generate diamond patterns, which represent 0.025% of all possible four-gene topologies. By systematically varying the interaction strengths within these GRNs (while keeping topology constant), we observed that most variation within the diamond-like pattern arises by modifications relating to G3, a modulator of the core Turing-type mechanism (Fig. 5B). Next, we assessed whether the control of morphogenetic cell processes (division, polarity, and motility) can theoretically lead to the observed transition between the diamond- and chevron-like patterns. In real developing epithelia, different morphogenetic cell

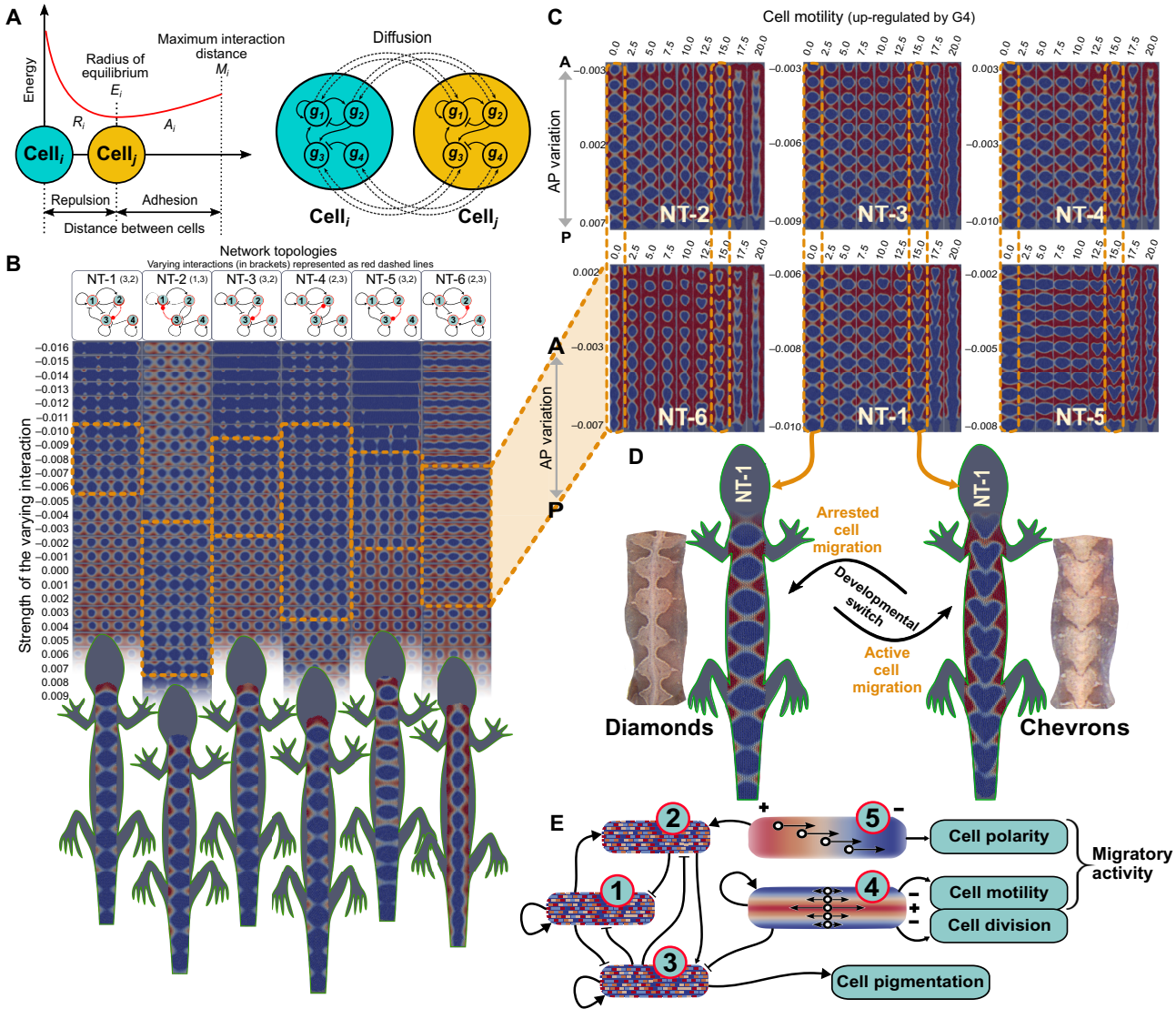

Fig. 5. In silico modeling of the *Anolis* dorsal patterning. (**A**) Core features of the cell-based modeling are biomechanical forces between interacting cells resulting in an energy landscape (left) and a GRN that is identical between all cells (right). Gene products can diffuse in the intercellular space (dashed lines) and hence affect the GRN dynamics of other cells. (**B**) An initial parametric exploration identified six candidate topologies (NT-1 to NT-6) of four-gene GRNs capable of generating diamond-like patterns. To reproduce naturally observed variation in the diamond shapes, we systematically varied the strength of the GRN connections that are responsible for the diamond-like pattern (red lines in GRNs). Orange dashed boxes show the range of parametric values that generate diamond-like variation. (**C**) Chevron-like patterns emerge when a fifth gene (G5) that provides AP polarity is added to any of the six NTs. Transition between chevrons and diamonds occurs as a result of variation in directional cell migration mediated through modifications in either cell motility (controlled by G4) or cell polarity (controlled by G5). By varying cell motility, a continuum of intermediate patterns (between diamonds and chevrons) appears. (**D**) The binary transition can be achieved either by disrupting cell motility (G4) or cell polarity (G5). (**E**) Schematic representation of the developmental processes underlying the dorsal patterning in *Anolis*. Spatial distributions of initial expression levels for each of the five genes (G1 to G5) on 2D epithelia are shown as red-blue color-coded (red: high expression; blue: low expression). Small black arrows within the G4 and G5 2D epithelia represent how these genes regulate the cell processes involved in cell migration: G5 provides an identical AP polarity to all cells, whereas G4 increases motility along the midline.

processes occur simultaneously, constituting a morphodynamic system. These systems exhibit qualitatively different properties than those where signaling and morphogenesis occur sequentially (*28*). Therefore, we model cell migration as part of the dynamical system (i.e., cells migrate and divide as they differentiate) rather than as a separate and independent process that transforms one fully formed pattern into another. Thus, we allowed each of the genes (G1 to G5) of our in silico developmental system to control one of these cell behaviors and evaluated the resulting gene expression patterns.

Our simulations demonstrate that chevron-like motifs can emerge when cell motility is more active along the midline (up-regulated by a gene with a transversal expression gradient, i.e., G4), and cells become polarized along the anteroposterior (AP) axis (up-regulated by a gene with an AP expression gradient, i.e., G5; Fig. 5, C and D). When cells exhibit decreased motility (G4) or polarity (G5), both potentially related to *CCDC170* function, they are unable to migrate according to these two gradients. As a result, no chevrons form, and instead, a diamond-like pattern emerges (Fig. 5E). These results support that, in principle, a functional difference in the proteins encoded by the two *CCDC170* alleles, causing the differences in cell polarity or motility observed in vitro (*23*), could act as a single genetic switch to regulate the transition between the two morphs.

DISCUSSION

Our finding that the switch between two distinct patterning morphs is regulated by a single gene is consistent with the frequent evolutionary transitions in animal color patterns. For example, a recent study in geckos showed that transitions between bands, spots, stripes, and plain patterns regularly occur (*29*), and diamond-like patterning has repeatedly evolved in lizards and snakes (*19*, *30*, *31*). These transitions between alternate phenotypes can be highly adaptive [e.g., in camouflage; (*32*)] and may therefore facilitate population persistence during rapid ecological disturbance (e.g., anthropogenic change). Besides its adaptive value, such repeated, convergent evolution of animal patterning suggests that these discrete phenotypes are highly accessible and, hence, that only minimal changes in their underlying developmental mechanism are necessary to evolve novel patterns. The stability of the diamond-like pattern against other model parameter perturbations in silico demonstrates that the proposed developmental mechanism exhibits the balance between robustness and lability that are known to promote evolvability (*33*).

CCDC is a large, widespread family of structural proteins (*34*), and for many members, it has been demonstrated that they tend to function in a redundant, exchangeable fashion (*35*). It is therefore conceivable that genetic variation in other *CCDC* genes or other genes that influence cell migration could lead to a similarly drastic switch in pigmentation patterning. The difference in expression of *CCDC170* between male and female embryos may indicate the presence of a threshold mechanism, further increasing the number of mutational targets that enable transitions between chevrons and diamonds. Yet, the genetic linkage and associated coexpression between *CCDC170* and the *Estrogen receptor 1* gene may explain why polymorphisms involving diamond patterns are more common in females than in males. Female pattern polymorphism has been gained or lost at least 28 times in the genus *Anolis* (*19*), but diamonds can also be found in male *Anolis* lizards (e.g., *Anolis bahorucoensis*). Such evolutionary lability, which manifests in frequent evolutionary transitions, is the hallmark of a highly evolvable developmental architecture with multiple ways of generating discrete, alternative phenotypes.

MATERIALS AND METHODS

Animal husbandry

Twenty-four female and eight adult male *A. sagrei* lizards were collected in Palm Coast, Florida in April 2016 and established as breeding stock at the animal facility at Lund University. The genetic mapping was performed on the wild-caught parental generation (F0) and two laboratory-reared generations (F1 and F2). No intergenerational crosses were set up. Each one male and three females were housed in an 80-liter cage (Wham Crystal box with mesh on top, 590 mm by 390 mm by 415 mm). Males were regularly swapped between cages of the same generation to increase the spread of parentages. Note that males can be carriers of all *CCDC10* genotypes (DD, Dc, and cc) but invariantly exhibit the chevron phenotype. Females were distributed to breeding groups of their generation randomly with respect to their phenotype and genotype. All cages were enriched with twigs, hiding areas, basking spots, a water bowl, and plastic cups with moist vermiculite for oviposition. Adult lizards were kept at a light cycle of 12-hour light:12-hour dark at room temperature of 24°C at day and 20°C at night and given access to basking lights (60 W) for 10 hours/day and an ultraviolet (UV) light (EXO-TERRA 10.0 UVB fluorescent tube) for 6 hours/day. During winter time (December to February), animals were kept at cooler temperatures (20°C at day and 16°C at night) with shorter light periods (10-hour light:14-hour dark; 8-hour basking light and 4-hour UV light daily). Mealworms and crickets were provided ad libitum and dusted with vitamins once per week. Eggs were collected every day and incubated at 26°C in individual small plastic containers filled two-thirds with moist vermiculite (5:1 vermiculite:water volume ratio) and sealed with cling film.

Genetic mapping

To increase the statistical power of the genetic mapping, we selected female individuals from three generations for whole-genome sequencing of pooled DNA samples. In total, we used 24 individuals of the F0 generation (15 diamond and 9 chevron), 97 of the F1 generation (67 diamond and 30 chevron), and 30 of the F2 generation (18 diamond and 12 chevron). All tissue samples were collected according to the Lund University Local Ethical Review Process. Genomic DNA was extracted from individual tail tips using the DNeasy Blood & Tissue Kit (Qiagen, USA) according to the manufacturer's instructions. DNA concentrations and purity in terms of protein contamination were quantified using NanoDrop, and individual DNA extractions were pooled at equimolar concentrations. The concentrations of the final DNA pools were assessed by the Qubit dsDNA BR Assay Kit, and DNA integrity was assessed using agarose gel electrophoresis. Final DNA pools were submitted for library preparation {NEBNext DNA Library Prep Kit; short-insert [350 base pairs (bp)] libraries} and sequencing (Illumina HiSeq X platform) to NOVOGENE Ltd. (Hong Kong). All pools were sequenced at an effective coverage of at least twice the number of individuals per pool (table S5).

Raw reads were quality-controlled using FastQC (version 0.11.8; www.bioinformatics.babraham.ac.uk/projects/fastqc/) and trimmed using Trimmomatic [version 0.36; (*36*)] using the following settings: TRAILING = 15, SLIDINGWINDOW = 4:20, and MINLEN = 30. Only read pairs in which both reads survived the trimming were

retained. Clean reads were aligned to the *A. sagrei* reference genome version 2.1 (*37*) using bwa-mem with default settings [version 0.7.1; (*38*)]. SNP calling was performed using the mpileup command (*39*) in the package samtools (version 1.10). Only SNPs with a Phred quality score of 20 or higher and a minimum coverage of five reads across all pools were considered. We discarded SNPs located in indels or within a 5-bp region surrounding indels. An upper threshold of twice the target coverage (1× per allele) was imposed to exclude regions with unusually high coverage, which are likely repetitive sequences. This resulted in a total of 58,709,334 SNPs that were included in the genetic differentiation (fixation index, F_{ST}) and association [Cochran-Mantel-Haenszel (CMH)] tests. For detailed information on sequencing statistics, see table S5.

To investigate genetic differentiation between pools of diamond and chevron individuals, we estimated the fixation index (F_{ST}) of each allele using the software PoPoolation2 (*40*). We first considered the F_{ST} values between pools of diamond versus chevron within each generation (F0, F1, and F2; fig. S2). To increase the resolution of the analysis, we present the median of all F_{ST} values between all combinations of pools of diamond versus chevron in the main text (intra- and intergenerational; Fig. 2). We present all F_{ST} values summarized over sliding windows with each window containing 100 SNPs and a step size of 25 SNPs. We summarized over a certain number of SNPs rather than a certain number of base pairs because the former allows for a more biologically meaningful interpretation. Alternative window sizes of 20 SNPs (5 SNP steps) and 200 SNPs (50 SNP steps) produced qualitatively identical results with one clear outlier peak. The exact position of the 44-kb candidate region was determined by locating the core region of the peak and extending along the scaffold until the F_{ST} values of the combined generations in a 100 SNP window dropped below 0.15 and extended for 10 windows on each side (scaffold_1: 279,264,376 to 279,308,704).

We further characterized the candidate region by calculating its nucleotide diversity π (*41*) using the software PoPoolation (*42*) in sliding windows of 10 kb (2.5-kb steps). We calculated nucleotide diversity π only for the F1 generation because these pools had the largest sample sizes and therefore the lowest noise levels. To visualize the distribution of major allele frequencies across all individual pools, we extracted all biallelic SNPs of the candidate region (N = 1923). Major allele frequencies were averaged between the two technical replicates of the F2 generation (see below). To exclude SNPs that were nearly fixed across all pools, we excluded SNPs with major allele frequencies above 0.7 in all pools (N = 845). We also excluded SNPs for which the major allele was absent in at least one pool (N = 11). The major allele frequencies of the remaining 1067 SNPs were plotted as heatmaps.

To investigate the association of SNPs with phenotypes, we used a CMH test (*43*, *44*) of association as implemented in PoPoolation2. This performs repeated tests of independence for every SNP and leverages the repeated contrasts of our experimental design. To not violate the assumptions of the test, we applied this test to intra-generational contrast only.

We reasoned that the F2 generation should be relatively depleted of genetic variation and should therefore have the highest power to detect the genetic loci underlying the pigmentation pattern polymorphism. We therefore sequenced the two pools in two technical replicates. In the F_{ST}-based analysis, we derived a single F_{ST}-value by deriving the median of all F_{ST} values from intra- and intergenerational Chevron-Diamond pairs. For those pairs including the F2 generation, F_{ST} values were calculated for each replicate, and the mean of both replicates was included in the calculation of a single F_{ST} value. In the CMH test, we derived P values from two separate tests, each including one of the two technical replicates: [(i) F0 Chevron versus F0 Diamond; F1 Chevron versus F1 Diamond; F2 Chevron rep1 versus F2 Diamond rep1] and [(ii) F0 Chevron versus F0 Diamond; F1 Chevron versus F1 Diamond; F2 Chevron rep2 versus F2 Diamond rep2]. We summarized P values of both CMH tests by calculating their arithmetic mean.

To test whether the candidate region is associated with an inversion, we used the software BreakDancer [version 1.4.5; (*45*)] with default settings on alignment files (bam files) of the F1 Diamond and F1 Chevron pools because these include the largest numbers of individuals.

Molecular and phylogenetic characterization of the two *CCDC170* alleles

To confirm the genotypes inferred by the pool-seq approach, we Sanger-sequenced *CCDC170* cDNA from 10 embryos, which confirmed the presence of two alleles. Full-length protein-coding sequences were curated for each allele (GenBank accession IDs: MZ268124 and MZ268125). These were submitted to a coiled-coil domain prediction tool (*46*) that uses hidden Markov models to characterize their domain structure and likely dimerization characteristics. Together with protein sequences of other reptile and bird species downloaded from public databases (table S3), we inferred the molecular phylogeny of *CCDC170*. Alignments were built using MUSCLE (*47*), and maximum likelihood and neighbor-joining phylogenetic trees were inferred using MEGA X (*48*). In addition, we used an alignment of all *Anolis CCDC170* nucleotide sequences to infer patterns of selection acting on protein sequences. We used codeml in the software package PAML [version 4.9; (*49*)] for maximum likelihood estimations of the numbers of nonsynonymous substitutions per nonsynonymous site (dN) and the number of synonymous substitutions per synonymous sites (dS), as well as their ratios (ω = dN/dS) for each branch (free-ratio model).

Genotyping and molecular sexing

Genotyping and molecular sexing were performed on DNA extracted from individual lizards as described above in the case of adult lizards and using the Arcturus PicoPure DNA Extraction Kit (Applied Biosystems). To assess the strength of association of SNPs in the candidate region with pigment patterning, we designed a genotyping assay. We targeted a SNP in exon 2 of the *CCDC170* gene (position scaffold_1:279,265,282) whose diamond allele constitutes a recognition site for the restriction enzyme Taq I. We used PCRs to amplify a 710-bp fragment including the allele-specific recognition site: primer forward: 5'-AAACGGAGCATCCATGACACT-3′; primer reverse: 5'-ATCTCATTACTGCCAGCACAC-3′.

PCR products were digested with Taq I, and genotypes were assessed by gel electrophoresis (homozygote chevron: one 710-bp band; homozygote diamond: one ~350-bp band; heterozygote: one ~350- and one 710-bp band).

Morphological sexing can be ambiguous for embryonic *Anolis*. We therefore applied molecular sexing using the primers AcarB previously developed [originally for *Anolis carolinensis*; (*50*)]. The primers target a male-specific fragment of 238 bp located on the Y chromosome. We first tested the accuracy of the molecular sexing on a set of 9 adult males and 24 adult females. After raising the annealing

temperature from the originally described 55°C (*50*) to 60°C, we confirmed that a 238-bp band was consistently generated in PCRs using male DNA but absent using female DNA.

In situ hybridization

To visualize gene expression of *CCDC170* and *ESR1* in *A. sagrei* embryos, we used whole-mount in situ hybridizations. To prepare RNA probes for *CCDC170* and *ESR1*, total RNA from a single embryo at stage 5 was extracted using the RNeasy Micro Kit (Qiagen) and reverse-transcribed into cDNA using SuperScript III (Invitrogen, Carlsbad, USA) following the instructions of the 3'-RACE System (Invitrogen, Carlsbad, USA; including RNase treatment of final cDNA). Primers were designed on the basis of genomic sequences to amplify partial cDNAs of *CCDC170* and *ESR1* and to include promoter sequences of SP6 (forward primer) or T7 (reverse primer) RNA polymerases [*CCDC170* fragment (985 bp): forward: 5'-ATTTAGGTGACACTATAGGTCTGCACAATGCATTCA-3′; reverse: 5'-TAATACGACTCACTATAGGGAACCGTGTTTTAATGCTG-3′; *ESR1* fragment (1251 bp): forward: 5'-ATTTAGGTGACACTATAGAGGCCGTATGTTGAAACA-3′; reverse: 5'-TAATACGACTCACTATAGGGATTTCCCTCTTCTTGCTTG-3′]. The obtained PCR fragments were used as templates for riboprobe synthesis using the DIG RNA Labeling Kit (Roche, Mannheim, Germany) with T7 RNA polymerases for antisense probes and SP6 for sense probes (as negative controls).

We targeted embryos at early [4 to 6 days post oviposition (dpo)], intermediate (9 to 11 dpo), and late (13 to 15 dpo) stages of development. Eggs were dissected in nuclease-free phosphate-buffered saline (PBS) and immediately fixed in 4% paraformaldehyde at 4°C for 12 to 24 hours. Embryos were transferred to methanol through a dilution series in PBS and stored at −20°C. In situ hybridization was performed as previously described (*51*). Expression patterns were documented using a Nikon stereo microscope (Nikon SMZ18) with the imaging software NIS-Elements BR 5.02.00. Observed expression patterns for each gene were confirmed in independent experiments on at least three embryos per stage.

Quantitative polymerase chain reaction

To assess the level of (co-)expression of *CCDC170* and *ESR1* during embryonic development in relevant tissues, we used the following approach. We dissected *A. sagrei* embryos at 7, 11 and 15 dpo corresponding to developmental stages 7, 11, and 13 (*52*) in nuclease-free PBS; collected their tails for genotyping and molecular sexing (see above); and stored embryos in RNA*later* (Qiagen) at −80°C. Hemipenes and dorsal tissues were dissected in RNA*later* using fine needles and capsulotomy scissors and immediately subjected to RNA extraction and cDNA synthesis as described above. Equimolar amounts of cDNA of each sample were used as templates in qPCRs for three genes (*GAPDH* as reference gene for internal normalization and *CCDC170* and *ESR1* as target genes), and each gene/sample combination was performed in three technical replicates. We used the following primers, all spanning at least two exons of the target gene: *GAPDH*: forward, 5'-CATGTTTGTGATGGGTGT-3′; reverse, 5'-ATGTTCTGAGAAGCTCCT-3′ (232-bp amplicon); *CCDC170*: forward, 5'-GAGTCTGAAGAGATCAAG-3′; reverse, 5'-GCTTTTGATTCCACCTCA-3′ (225-bp amplicon); *ESR1*: forward, 5'-GGTGGAATTCGAAAAGAC-3′; reverse, 5'-TGCTAGGGTCATATTCTG-3′ (245-bp amplicon). qPCRs were processed using a Bio-Rad CFX96 instrument implementing a balanced plate design (i.e., experimental groups were spread across plates to minimize plate effects). C_q values were determined using the regression mode in the Bio-Rad CFX Maestro software and exported for analyses in R (*53*). A small number of PCRs failed [high C_q values that strongly deviated from the other two technical replicates (SD >> 1)] and were therefore excluded from the analyses. Relative expression of the target genes *CCDC170* and *ESR1* was calculated using the following formula (*54*)

$$\text{Relative expression (target)} = 2^{-[\text{Cq(target)}-\text{Cq(reference)}]}$$

We used partial correlations in the R package ppcor (*55*) to assess coexpression between *CCDC170* and *ESR1* by accounting for the expression of the reference gene *GAPDH* (this excludes the possibility that coexpression is an artifact of normalizing with the same reference gene). Linear models in combination with analysis of variances (ANOVAs) were used to statistically assess the expression difference between experimental groups.

In silico modeling of pattern formation

The mathematical model is based on (*56*) and comprises a 2D elongated epithelium composed of N_c randomly distributed spherical, motile cells ($10^3 < N_c < 10^4$), each with spatial coordinates (x_i, y_i) and a specific radius of equilibrium E_i. If the distance between the cells i and j is smaller than E_i ($D_{ij} < E_i$), then a repulsion force R_i prevents cells to occupy the same position. If ($M_i > D_{ij} > E_i$), then an adhesion force A_i ($A_i \leq R_i$) keeps cells attached to each other, ensuring the continuity of the epithelial layer (M_i is the maximum distance at which two cells can physically interact). These parameters are kept equal for all cells and set to values that reproduce the basic biomechanical motion of cells ($E_i = 1.0$, $M_i = 2.6 \times E_i$, $A_i = 1.0$, and $R_i = 1.6\ \forall\ i \in \{1, N_c\}$). Cell motion is computed assuming Langevin overdamped dynamics, and thus, the force vector $\boldsymbol{F_i}$ applied to the cell i will be

$$\overrightarrow{F_i} = \boldsymbol{r} + \sum_{j=1}^{N_i} \overrightarrow{F_{ij}} \tag{1}$$

where the first term $\boldsymbol{r}$ is a small random vector that introduces a certain amount of noise to the system, and the second term is the sum of all the local mechanical interactions with other neighboring cells. The number of neighboring cells (N_i) that surround and can potentially interact with cell i is dynamically determined by means of a Delaunay triangulation (*57*). Thus, the strength and direction of the local interaction between the cell i (the one for which the force is being calculated) and each of its neighboring cells j depend on the aforementioned force-related parameters and on the Euclidean distance (D_{ij}) between the two cells i and j, namely

$$\overrightarrow{F_{ij}} = \widehat{\boldsymbol{u}_{ij}}(A_i \cdot |E_i - D_{ij}|) \Leftrightarrow D_{ij} > E_i \tag{2}$$

$$\overrightarrow{F_{ij}} = \widehat{\boldsymbol{u}_{ij}}(R_i \cdot |E_i - D_{ij}|) \Leftrightarrow D_{ij} < E_i \tag{3}$$

$$\overrightarrow{F_{ij}} = 0 \Leftrightarrow (D_{ij} = E_i) \vee (D_{ij} \geq M_i) \tag{4}$$

with $\hat{\boldsymbol{u}}_{ij}$ being the unitary vector that goes from the cell i to cell j.

Each cell also contains N_g gene products (transcription factors) that have continuous concentrations [vector $\boldsymbol{G} = (g_1, \ldots, g_{Ng})$; $g_i \geq 0\ \forall\ i$]. The initial state of $\boldsymbol{G}$ ($\boldsymbol{G_0}$) depends on a cell's position within

the epithelium: gene 1 (G1) and G2 (which form the core Turing-type mechanism) and G3 are initially expressed at random: $g_{(0)1-3} \sim U(0,1)$. G4 forms a transversal gradient whose maximal expression is along the midline and decreases toward the lateral borders: $g_{(0)4i} = e^{-|yi|}$, and G5 forms an AP gradient according to $g_{(0)5i} = e^{-|xi|}$. While these gradients are biologically highly plausible [e.g., retinoic acid follows an AP gradient, and Bmp/Shh follows a transversal gradient in all vertebrate embryos (*58*)], none of them alone nor a simple combination of them provide sufficient positional information to determine the patterning phenotypes investigated here.

Over developmental time, gene products derived from G1 to G5 regulate the expression of each other by binding to cis-regulatory sequences on gene promoters. These regulatory interactions conform to a GRN, which is identical for all cells and encoded in the $N_g \times N_g$ matrix $\boldsymbol{B}$. Each B_{ik} element of the $\boldsymbol{B}$ matrix represents the effect of gene k on the transcription of gene i: ($B_{ik} > 0$ activation; $B_{ik} < 0$ inhibition). The resulting GRN dynamics produce changes in gene concentration over developmental time. In addition, gene products can diffuse between cells with a diffusion rate D_i ($0 < D_i < 1$), defining a multicellular reaction-diffusion system where the change in concentration of a gene i in a cell j is calculated as

$$\frac{\partial g_{ij}}{\partial t} = \frac{R(h_{ij})}{K_M + R(h_{ij})} - \mu g_{ij} + \xi + D_i \nabla^2 g_{ij}, \text{where } h_{ij} = \sum_{k=1}^{Ng} B_{ik} g_{kj} \quad (5, 6)$$

and $R(h_{ij})$ is the Ramp function [$R(x) = x, \forall\, x \geq 0$ and 0 otherwise], which prevents negative concentrations in gene products. K_M is the Michaelis-Menten coefficient ($K_M = 1$), which introduces saturating dynamics in gene expression, and the term μ_i ($0 < \mu_i < 1$) is a gene-specific decay term. The term $\xi \sim U(-10^{-2}, 10^{-2})$ introduces a certain amount of noise to the system to prevent unstable solutions.

Besides reaction and diffusion, gene products are also able to modulate certain basic cell behaviors. If a gene product i plays a role in cell division [$g_i(\text{div}) > 0$], then the probability p_j^{MIT} of a cell j to undergo mitosis will depend on the concentration of that gene

$$p_j^{\text{MIT}} = 1 - e^{-\sum_{i=1}^{Ng} g_{ij} \cdot g_i(\text{div})} \Leftrightarrow g_i(\text{div}) > 0 \quad (7)$$

By default, each daughter cell $N_c + 1$ is identical to its mother cell and appears at random orientation relative to it ($D_{i,Nc+1} = E_i/2$), but if $g_i(\text{pdiv}) > 0$, the new cell arises in the direction where the local gradient of the gene product i is higher [i.e., polarized cell division by an active positioning of the mitotic spindle (*59*)]. Cells are also able to undergo directional movements by means of active cytoskeletal dynamics. The ability of a gene i to trigger the emission of pseudopodia (e.g., via microtubule polymerization) is captured by the parameter $g_i(\text{mov})$, which determines the module of the vector of directional, active cell movement. The direction of this vector is set by default at random, but if there exists a gene product with polarizing effect [$g_i(\text{pol}) > 0$], the cell will tend to migrate toward the direction where the local gradient of such polarizing morphogen(s) is highest (i.e., chemotaxis). The direction of such chemotactic cell movement (the vector $\boldsymbol{Qi}$) is thus calculated as

$$\overrightarrow{Q_i} = \frac{\sum_{j=1}^{Nc}\sum_{k=1}^{Ng}(g_{ki} - g_{kj})}{|\sum_{j=1}^{Nc}\sum_{k=1}^{Ng}(g_{ki} - g_{kj})|} \cdot \sum_{j=1}^{Ng} g_j(\text{mov}) \quad (8)$$

and introduced as an independent term in the motion equation Eq. 1, which now becomes

$$\overrightarrow{F_i} = r + \overrightarrow{Q_i} + \sum_{j=1}^{N_i} \overrightarrow{F_{ij}} \quad (9)$$

In silico modeling of the diamond-like pattern

Our initial goal was to establish the minimal and necessary conditions for the diamond pattern to emerge. Note that because our goal was to model the principles of pattern formation, we did not fine-tune the model to capture all aspects of the observed patterns in *A. sagrei* (e.g., left-right asymmetries). We started by setting a basic two-gene Turing-type mechanism as the GRN core that is capable of creating AP periodicity ($B_{1,1} = 0.16$, $B_{1,2} = -0.08$, and $B_{2,1} = 0.12$). Because diamonds are more complex than simple stripes (thus requiring extra genes), we introduced in the GRN a third gene (G3), whose initial expression is also random, and a transversally expressed gene (G4). Given that we had no a priori expectation about how these extra genes would interact with the core Turing-type mechanism, we exhaustively tried all NTs ($n = 3^5 = 243$) by which G3 and G4 can be linked with G1 and G2 to assess which NT generates diamond-like patterns. Such topological exploration was performed using $|B_{ij}| = \{1,0\}$, and only the behavior of cell division was included. Simulations stopped after the number of cells was doubled. To be considered diamond-like, the normalized expression patterns of at least one gene at the end of simulation must be a sequence of evenly sized rhombus-shaped elements that contact the midline, a criterion that was fulfilled by six different NTs. In all six NTs, the expression pattern of G3 reflected the actual pigmentation pattern, suggesting that G3 represents the gene that is directly controlling pigment production or regulating chromatophore sorting (in case of a prepatterning mechanism).

After identifying these six NTs, we next introduced a more fine-grained and systematic (log-)variation in their interaction strengths ($-1 < B_{ij} < +1\ \forall\ i > 2$ and $j > 2$) to create a theoretical morphospace of diamond-like patterns. This morphospace exploration revealed that the different NTs have different sensitivities to parametric changes, with diamonds occurring at relatively weak interaction strengths ($-0.016 < B_{ij} < +0.008$). In these regions, we performed parametric (linear) zoom-ins to reproduce different types of diamonds from the "closed" ones, which contact the midline, to the more "open" diamonds that approach a straight bar along the midline (see fig. S1). These simulations suggest that small variations in a single parameter (i.e., a single genetic locus) suffice to account for most of the naturally observed variation in the diamond patterns (fig. S1) (*60*)).

Exploring the diamond to chevron transition in silico

In previous simulations, only reaction diffusion and cell division (both nondirectional processes) were considered, and thus, the resulting diamonds were anteroposteriorly symmetric. In contrast, chevrons are asymmetric with respect to the AP axis, which suggest that some directional cell process(es) must be involved in their development. We therefore introduced a fifth gene (G5) to the GRNs that exhibits an AP expression gradient. Although empirical data suggest that the diamond-chevron transition is controlled by a single gene (see the Results section), we address this question in an unbiased, heuristic manner by introducing two potential directional cell processes to the system:

1) Oriented cell division. In contrast to previous simulations describe above, we allow cell division to take place parallel to the AP gradient (G5), perpendicular to it (G4), or following the gradient of one of the periodically expressed genes (G1). This was achieved by setting the $g_i(\text{pdiv})$ parameter, which determines which (if any) morphogen orients the mitotic spindle, to $g_{\{1,4,5\}}(\text{pdiv}) = 1$.

2) Cell migration. It occurs by a combination between increased cell motility (a genetically up-regulated cytoskeletal dynamics) and cell polarity that provides cells with a direction to follow. Cells can become polarized toward regions with higher morphogen concentration or against them (both possibilities were explored). Thus, we allow each of the five genes to be involved in cell motility and/or polarity [respectively, $g_{\{1,2,3,4,5\}}(\text{mot}) \neq 0$ and $g_{\{1,2,3,4,5\}}(\text{pol}) = \{1,-1\}$].

Note that the gene regulating cell polarity per se and the gene regulating cell motility do not have to be the same, which allows us to discriminate between their causal effects. For the sake of simplicity, only NT-1 was used for this experiment, summing up a total of $6^2 \times 4$ (division modes) $\times$ 2 (morphogen attraction or avoidance) = 288 possibilities. Simulations revealed that chevron-like structures only appear when cell migration is more active along the midline (i.e., cell motility is up-regulated by G4), and cells are polarized along the AP morphogen gradient set up by G5. Oriented cell division has no morphogenetic effect, likely because other larger morphogenetic movements quickly overcome the small deviations in the daughter cells' positions.

To better understand the biomechanics of the diamond-chevron transition, we gradually varied the migration strength [$g_4(\text{mov}) = \{0,20\}$ at 2.5 intervals] while keeping the required AP polarization [$g_5(\text{pol}) = -1$]. We did this for each of the six presumptive NTs with similar results (results are shown in Fig. 5C). Simulations reveal that the diamond-chevron transition can be linked to changes in the rate of cell migration: When G4 up-regulates cell motility, the bulk of cells close to the midline becomes displaced in the AP direction following the G5 polarizing gradient. The net displacement becomes smaller as cells approach the borders of the epithelium, a dynamic that closely resembles a highly viscous fluid. This, in turn, produces a sheering force that deforms the central region of the diamonds, turning them into chevrons. The core Turing-type mechanism likely stabilizes the deformation by preventing the coalescence of adjacent chevrons. However, this buffering mechanism is not sufficient when cell migration is too large: over $g_4(\text{mov}) \geq 17.5$, chevron formation is disrupted, and epithelia show no distinct expression pattern.

Overall, these results suggest that the chevron-diamond transition can be achieved by means of two nonmutually exclusive genetic triggers, both related to cytosketal dynamics (and hence potentially to allelic variation in *CCDC170*). One is by disrupting the cells' sensitivity to the AP morphogen gradient, thus impeding cell polarity (related to G5), and the other is by arresting the up-regulation of cell motility by the transversally expressed morphogen (related to G4). If any of these two mechanisms of cell migration is disrupted, then cells fail to assembly into the chevron-like pattern, which is apparent in the expression patterns of G3.

SUPPLEMENTARY MATERIALS

Supplementary material for this article is available at https://science.org/doi/10.1126/sciadv.abm2387

View/request a protocol for this paper from *Bio-protocol*.

REFERENCES AND NOTES

1. A. M. Turing, The chemical basis of morphogenesis. *Philos. Trans. R. Soc. Lond. B Biol. Sci.* **237**, 37–72 (1952).
2. S. Kondo, T. Miura, Reaction-diffusion model as a framework for understanding biological pattern formation. *Science* **329**, 1616–1620 (2010).
3. S. Kondo, R. Asal, A reaction-diffusion wave on the skin of the marine angelfish Pomacanthus. *Nature* **376**, 765–768 (1995).
4. H. Meinhardt, D. R. Fowler, P. Prusinkiewicz, *Algorithmic Beauty of Sea Shells* (Springer-Verlag, 2003).
5. S. Sick, S. Reinker, J. Timmer, T. Schlake, WNT and DKK determine hair follicle spacing through a reaction-diffusion mechanism. *Science* **314**, 1447–1450 (2006).
6. J. Raspopovic, L. Marcon, L. Russo, J. Sharpe, Modeling digits. Digit patterning is controlled by a Bmp-Sox9-Wnt Turing network modulated by morphogen gradients. *Science* **345**, 566–570 (2014).
7. R. Sheth, L. Marcon, M. F. Bastida, M. Junco, L. Quintana, R. Dahn, M. Kmita, J. Sharpe, M. A. Ros, Hox genes regulate digit patterning by controlling the wavelength of a Turing-type mechanism. *Science* **338**, 1476–1480 (2012).
8. I. Salazar-Ciudad, J. Jernvall, A computational model of teeth and the developmental origins of morphological variation. *Nature* **464**, 583–586 (2010).
9. J. E. Moustakas-Verho, R. Zimm, J. Cebra-Thomas, N. K. Lempiäinen, A. Kallonen, K. L. Mitchell, K. Hämäläinen, I. Salazar-Ciudad, J. Jernvall, S. F. Gilbert, The origin and loss of periodic patterning in the turtle shell. *Development* **141**, 3033–3039 (2014).
10. M. Yamaguchi, E. Yoshimoto, S. Kondo, Pattern regulation in the stripe of zebrafish suggests an underlying dynamic and autonomous mechanism. *Proc. Natl. Acad. Sci. U.S.A.* **104**, 4790–4793 (2007).
11. A. Nakamasu, G. Takahashi, A. Kanbe, S. Kondo, Interactions between zebrafish pigment cells responsible for the generation of Turing patterns. *Proc. Natl. Acad. Sci. U.S.A.* **106**, 8429–8434 (2009).
12. R. T. Liu, S. S. Liaw, P. K. Maini, Two-stage Turing model for generating pigment patterns on the leopard and the jaguar. *Phys. Rev. E Stat. Nonlin. Soft Matter Phys.* **74**, 011914 (2006).
13. J. D. Murray, A Pre-pattern formation mechanism for animal coat markings. *J. Theor. Biol.* **88**, 161–199 (1981).
14. M. E. Rawles, Origin of pigment cells from the neural crest in the mouse embryo. *Physiol. Zool.* **20**, 248–266 (1947).
15. M. E. Bronner, N. M. LeDouarin, Development and evolution of the neural crest: An overview. *Dev. Biol.* **366**, 2–9 (2012).
16. M. Reyes, K. Zandberg, I. Desmawati, M. E. de Bellard, Emergence and migration of trunk neural crest cells in a snake, the California Kingsnake (Lampropeltis getula californiae). *BMC Dev. Biol.* **10**, 52 (2010).
17. E. H. Barriga, E. Theveneau, In vivo neural crest cell migration is controlled by "Mixotaxis". *Front. Physiol.* **11**, 586432 (2020).
18. J. C. M. Meiring, B. I. Shneyer, A. Akhmanova, Generation and regulation of microtubule network asymmetry to drive cell polarity. *Curr. Opin. Cell Biol.* **62**, 86–95 (2020).
19. E. A. D. Paemelaere, C. Guyer, F. S. Dobson, A phylogenetic framework for the evolution of female polymorphism in anoles. *Biol. J. Linn. Soc.* **104**, 303–317 (2011).
20. S. Kurland, C. W. Wheat, M. Paz Celorio Mancera, V. E. Kutschera, J. Hill, A. Andersson, C. J. Rubin, L. Andersson, N. Ryman, L. Laikre, Exploring a Pool-seq-only approach for gaining population genomic insights in nonmodel species. *Ecol. Evol.* **9**, 11448–11463 (2019).
21. L. Truebestein, T. A. Leonard, Coiled-coils: The long and short of it. *Bioessays* **38**, 903–916 (2016).
22. A. K. Dunbier, H. Anderson, Z. Ghazoui, E. Lopez-Knowles, S. Pancholi, R. Ribas, S. Drury, K. Sidhu, A. Leary, L.-A. Martin, M. Dowsett, *ESR1* is co-expressed with closely adjacent uncharacterised genes spanning a breast cancer susceptibility locus at 6q25.1. *PLOS Genet.* **7**, e1001382 (2011).
23. P. Jiang, Y. Li, A. Poleshko, V. Medvedeva, N. Baulina, Y. Zhang, Y. Zhou, C. M. Slater, T. Pellegrin, J. Wasserman, M. Lindy, A. Efimov, M. Daly, R. A. Katz, X. Chen, The protein encoded by the CCDC170 breast cancer gene functions to organize the golgi-microtubule network. *EBioMedicine* **22**, 28–43 (2017).
24. J. Veeraraghavan, Y. Tan, X. X. Cao, J. A. Kim, X. Wang, G. C. Chamness, S. N. Maiti, L. J. N. Cooper, D. P. Edwards, A. Contreras, S. G. Hilsenbeck, E. C. Chang, R. Schiff, X. S. Wang, Recurrent ESR1-CCDC170 rearrangements in an aggressive subset of oestrogen receptor-positive breast cancers. *Nat. Commun.* **5**, 4577 (2014).
25. T. J. Sanger, B. K. Kircher, Model clades versus model species: Anolis lizards as an integrative model of anatomical evolution. *Methods Mol. Biol.* **1650**, 285–297 (2017).
26. L. Manukyan, S. A. Montandon, A. Fofonjka, S. Smirnov, M. C. Milinkovitch, A living mesoscopic cellular automaton made of skin scales. *Nature* **544**, 173–179 (2017).
27. K. J. Painter, G. S. Hunt, K. L. Wells, J. A. Johansson, D. J. Headon, Towards an integrated experimental-theoretical approach for assessing the mechanistic basis of hair and feather morphogenesis. *Interface Focus* **2**, 433–450 (2012).
28. I. Salazar-Ciudad, J. Jernvall, How different types of pattern formation mechanisms affect the evolution of form and development. *Evol. Dev.* **6**, 6–16 (2004).
29. W. L. Allen, N. Moreno, T. Gamble, Y. Chiari, Ecological, behavioral, and phylogenetic influences on the evolution of dorsal color pattern in geckos. *Evolution* **74**, 1033–1047 (2020).

30. J. Melville, S. K. Wilson, *Dragon Lizards of Australia* (Museum of Victoria, Melbourne, Australia, 2019).
31. J. D. Murray, M. R. Myerscough, Pigmentation pattern formation on snakes. *J. Theor. Biol.* **149**, 339–360 (1991).
32. E. D. Brodie III, Correlational selection for color pattern and antipredator behavior in the garter snake Thamnophis ordinoides. *Evolution* **46**, 1284–1298 (1992).
33. A. Wagner, Robustness and evolvability: A paradox resolved. *Proc. Biol. Sci.* **275**, 91–100 (2008).
34. A. Rose, S. J. Schraegle, E. A. Stahlberg, I. Meier, Coiled-coil protein composition of 22 proteomes—Differences and common themes in subcellular infrastructure and traffic control. *BMC Evol. Biol.* **5**, 66 (2005).
35. S. Mamoor, Multiple genes encoding coiled-coil domain-containing proteins are simultaneously differentially expressed in metastasis to the lung in a HER2+ mouse model of metastatic breast cancer. *OSF Preprints*, (2019).
36. A. M. Bolger, M. Lohse, B. Usadel, Trimmomatic: A flexible trimmer for Illumina sequence data. *Bioinformatics* **30**, 2114–2120 (2014).
37. A. J. Geneva, S. Park, D. Bock, P. de Mello, F. Sarigol, M. Tollis, C. Donihue, R. Graham Reynolds, N. Feiner, A. M. Rasys, J. D. Lauderdale, S. G. Minchey, A. J. Alcala, C. R. Infante, J. J. Kolbe, D. Schluter, D. B. Menke, J. B. Losos, Chromosome-scale genome assembly of the brown anole (*Anolis sagrei*), a model species for evolution and ecology. *bioRxiv*, 2021.09.28.462146 (2021).
38. H. Li, R. Durbin, Fast and accurate short read alignment with Burrows-Wheeler transform. *Bioinformatics* **25**, 1754–1760 (2009).
39. H. Li, A statistical framework for SNP calling, mutation discovery, association mapping and population genetical parameter estimation from sequencing data. *Bioinformatics* **27**, 2987–2993 (2011).
40. R. Kofler, R. V. Pandey, C. Schlotterer, PoPoolation2: Identifying differentiation between populations using sequencing of pooled DNA samples (Pool-Seq). *Bioinformatics* **27**, 3435–3436 (2011).
41. M. Nei, *Molecular Evolutionary Genetics* (Columbia Univ. Press, 1987).
42. R. Kofler, P. Orozco-terWengel, N. de Maio, R. V. Pandey, V. Nolte, A. Futschik, C. Kosiol, C. Schlötterer, PoPoolation: A toolbox for population genetic analysis of next generation sequencing data from pooled individuals. *PLOS ONE* **6**, e15925 (2011).
43. W. Cochran, Some methods for strengthening the common χ^2 tests. *Bioethics* **10**, 417 (1954).
44. N. Mantel, W. Haenszel, Statistical aspects of the analysis of data from retrospective studies of disease. *J. Natl. Cancer Inst.* **22**, 719–748 (1959).
45. X. Fan, T. E. Abbott, D. Larson, K. Chen, BreakDancer: Identification of genomic structural variation from paired-end read mapping. *Curr. Protoc. Bioinformatics* **45**, 15.6.1–15.6.11 (2014).
46. J. Trigg, K. Gutwin, A. E. Keating, B. Berger, Multicoil2: Predicting coiled coils and their oligomerization states from sequence in the twilight zone. *PLOS ONE* **6**, e23519 (2011).
47. R. C. Edgar, MUSCLE: Multiple sequence alignment with high accuracy and high throughput. *Nucleic Acids Res.* **32**, 1792–1797 (2004).
48. S. Kumar, G. Stecher, M. Li, C. Knyaz, K. Tamura, MEGA X: Molecular evolutionary genetics analysis across computing platforms. *Mol. Biol. Evol.* **35**, 1547–1549 (2018).
49. Z. Yang, PAML 4: Phylogenetic analysis by maximum likelihood. *Mol. Biol. Evol.* **24**, 1586–1591 (2007).
50. T. Gamble, D. Zarkower, Identification of sex-specific molecular markers using restriction site-associated DNA sequencing. *Mol. Ecol. Resour.* **14**, 902–913 (2014).
51. N. Feiner, Evolutionary lability in *Hox* cluster structure and gene expression in *Anolis* lizards. *Evol. Lett.* **3**, 474–484 (2019).
52. T. J. Sanger, J. B. Losos, J. J. Gibson-Brown, A developmental staging series for the lizard genus *Anolis*: A new system for the integration of evolution, development, and ecology. *J. Morphol.* **269**, 129–137 (2008).
53. R. C. Team (R Foundation for Statistical Computing, Vienna, Austria, 2020).
54. K. J. Livak, T. D. Schmittgen, Analysis of relative gene expression data using real-time quantitative PCR and the 2(-Delta Delta C(T)) Method. *Methods* **25**, 402–408 (2001).
55. S. Kim, ppcor: An R package for a fast calculation to semi-partial correlation coefficients. *Commun. Stat. Appl. Methods* **22**, 665–674 (2015).
56. M. Marin-Riera, M. Brun-Usan, R. Zimm, T. Välikangas, I. Salazar-Ciudad, Computational modeling of development by epithelia, mesenchyme and their interactions: A unified model. *Bioinformatics* **32**, 219–225 (2016).
57. S. Fortune, in *Computing in Euclidean Geometry* (World Scientific, 1992), vol. 1, pp. 193–233.
58. S. F. Gilbert, M. J. F. Barresi, *Developmental Biology* (2016).
59. E. M. Munro, G. Odell, Morphogenetic pattern formation during ascidian notochord formation is regulative and highly robust. *Development* **129**, 1–12 (2002).
60. R. M. Moon, A. Kamath, Re-examining escape behaviour and habitat use as correlates of dorsal pattern variation in female brown anole lizards, *Anolis sagrei* (Squamata: Dactyloidae). *Biol. J. Linn. Soc.* **126**, 783–795 (2019).
61. R. Calsbeek, L. Bonvini, R. M. Cox, Geographic variation, frequency-dependent selection, and the maintenance of a female-limited polymorphism. *Evolution* **64**, 116–125 (2010).
62. R. Calsbeek, C. Bonneaud, T. B. Smith, Differential fitness effects of immunocompetence and neighbourhood density in alternative female lizard morphs. *J. Anim. Ecol.* **77**, 103–109 (2008).
63. R. Calsbeek, R. M. Cox, An experimental test of the role of predators in the maintenance of a genetically based polymorphism. *J. Evol. Biol.* **25**, 2091–2101 (2012).
64. R. M. Cox, R. Calsbeek, An experimental test for alternative reproductive strategies underlying a female-limited polymorphism. *J. Evol. Biol.* **24**, 343–353 (2011).
65. A. M. Les, M. E. Gifford, J. S. Parmerlee, R. Powell, Do polymorphic female brown anoles (*Anolis sagrei*) differ in sprint speed or escape behavior? *Herpetologica* **70**, 47–55 (2014).
66. N. Feiner, K. L. Munch, I. S. C. Jackson, T. Uller, Enhanced locomotor performance on familiar surfaces is uncoupled from morphological plasticity in Anolis lizards. *J. Exp. Zool. A Ecol. Integr. Physiol.* **333**, 284–294 (2020).
67. S. Poe, A. Nieto-montes de oca, O. Torres-carvajal, K. de Queiroz, J. A. Velasco, B. Truett, L. N. Gray, M. J. Ryan, G. Köhler, F. Ayala-varela, I. Latella, A phylogenetic, biogeographic, and taxonomic study of all extant species of *Anolis* (Squamata; Iguanidae). *Syst. Biol.* **66**, 663–697 (2017).
68. M. Tollis, E. D. Hutchins, J. Stapley, S. M. Rupp, W. L. Eckalbar, I. Maayan, E. Lasku, C. R. Infante, S. R. Dennis, J. A. Robertson, C. M. May, M. R. Crusoe, E. Bermingham, D. F. DeNardo, S. T. T. Hsieh, R. J. Kulathinal, W. O. McMillan, D. B. Menke, S. C. Pratt, J. A. Rawls, O. Sanjur, J. Wilson-Rawls, M. A. Wilson Sayres, R. E. Fisher, K. Kusumi, Comparative genomics reveals accelerated evolution in conserved pathways during the diversification of anole lizards. *Genome Biol. Evol.* **10**, 489–506 (2018).

Acknowledgments: The genomic analyses were enabled by resources provided by the Swedish National Infrastructure for Computing (SNIC) at UPPMAX, partially funded by the Swedish Research Council through grant agreement no. 2018-05973. We thank M. Carneiro for constructive feedback on the manuscript. We thank D. Warner and T. Mitchell for assistance with collecting animals in the field. We thank two anonymous reviewers for constructive feedback. **Funding:** This work was supported by the John Templeton Foundation (no. 60501) to T.U., the Knut and Alice Wallenberg Foundation through a Wallenberg Academy Fellowship to T.U., the European Research Council through a Starting Grant (no. 948126) to N.F., the Swedish Research Council through a Starting Grant (no. 2020-03650) to N.F., and the NSF (nos. 1827647 and 1927156 to D.B.M. and no. 1927194 to A.J.G.). **Author contributions:** N.F. and T.U. conceived the study with input from M.B.-U., P.A., and R.P. N.F. and T.U. coordinated the study. A.J.G., S.P., and D.B.M. generated the reference genome. N.F. collected and analyzed genetic data with input from P.A. R.P. collected and analyzed phenotypic data with input from N.F. M.B.-U. performed theoretical modeling with input from N.F. and T.U. N.F., M.B.U., and T.U. wrote the manuscript with input from P.A. All authors approved the final manuscript. **Competing interests:** The authors declare that they have no other competing interests. **Data and materials availability:** All data needed to evaluate the conclusions in the paper are present in the paper and/or the Supplementary Materials. Pool sequencing data are available in the NCBI Sequence Read Archive (SRA) under BioProject PRJNA731327. Curated coding sequences of *A. sagrei CCDC170* alleles are deposited at GenBank (accession IDs: MZ268124 and MZ268125). qPCR data, alignments used in phylogenetic tree inference, and phenotyping data are available from the Dryad digital repository (https://doi.org/10.5061/dryad.cnp5hqc64). Code for the in silico modeling of pattern formation is available from the Zenodo digital repository (https://doi.org/10.5281/zenodo.5834386).

Submitted 10 September 2021
Accepted 13 January 2022
Published 9 March 2022
10.1126/sciadv.abm2387